Journal Name

ARTICLE

Experimental and Computational Studies of Criegee Intermediate Reactions with NH_3 and CH_3NH_2

Received 00th January 20xx,
Accepted 00th January 20xx

DOI: 10.1039/x0xx00000x

www.rsc.org/

Rabi Chhantyal-Pun,[a]* Robin J. Shannon,[a,g] David P. Tew,[b] Rebecca L. Caravan,[c] Marta Duchi,[a] Callum Wong,[a] Aidan Ingham,[a] Charlotte Feldman,[a] Max R. McGillen,[a] M. Anwar H. Khan,[a] Ivan O. Antonov,[c] Brandon Rotavera,[d,e] Krupa Ramasesha,[c] David L. Osborn,[c] Craig A. Taatjes,[c] Carl J. Percival,[f] Dudley E. Shallcross,[a] Andrew J. Orr-Ewing[a]

Ammonia and amines are emitted into the troposphere by various natural and anthropogenic sources, where they have a significant role in aerosol formation. Here, we explore the significance of their removal by reaction with Criegee intermediates, which are produced in the troposphere by ozonolysis of alkenes. Rate coefficients for the reactions of two representative Criegee intermediates, formaldehyde oxide (CH_2OO) and acetone oxide ($(CH_3)_2COO$) with NH_3 and CH_3NH_2 were measured using cavity ring-down spectroscopy. Temperature-dependent rate coefficients, k ($CH_2OO + NH_3$) = $(3.1 \pm 0.5) \times 10^{-20}$ T^2 exp $(1011 \pm 48 / T)$ cm^3 s^{-1} and k ($CH_2OO + CH_3NH_2$) = $(5 \pm 2) \times 10^{-19}$ T^2 exp $(1384 \pm 96 / T)$ cm^3 s^{-1} were obtained in the 240 to 320 K range. Both the reactions of CH_2OO were found to be independent of pressure in the 10 to 100 Torr (N_2) range, and average rate coefficients k ($CH_2OO + NH_3$) = $(8.4 \pm 1.2) \times 10^{-14}$ cm^3 s^{-1} and k ($CH_2OO + CH_3NH_2$) = $(5.6 \pm 0.4) \times 10^{-12}$ cm^3 s^{-1} were deduced at 293 K. An upper limit of $\leq 2.7 \times 10^{-15}$ cm^3 s^{-1} was estimated for the rate coefficient of the $(CH_3)_2COO + NH_3$ reaction. Complementary measurements were performed with mass spectrometry using synchrotron radiation photoionization giving k ($CH_2OO + CH_3NH_2$) = $(4.3 \pm 0.5) \times 10^{-12}$ cm^3 s^{-1} at 298 K and 4 Torr (He). Photoionization mass spectra indicated production of NH_2CH_2OOH and $CH_3N(H)CH_2OOH$ functionalized organic hydroperoxide adducts from $CH_2OO + NH_3$ and $CH_2OO + CH_3NH_2$ reactions, respectively. *Ab initio* calculations performed at the CCSD(T)(F12*)/cc-pVQZ-F12//CCSD(T)(F12*)/cc-pVDZ-F12 level of theory predicted pre-reactive complex formation, consistent with previous studies. Master equation simulations of the experimental data using the *ab initio* computed structures identified submerged barrier heights of -1.9 ± 0.1 kJ mol^{-1} and -22.4 ± 0.2 kJ mol^{-1} for the $CH_2OO + NH_3$ and $CH_2OO + CH_3NH_2$ reactions, respectively. The reactions of NH_3 and CH_3NH_2 with CH_2OO are not expected to compete with its removal by reaction with $(H_2O)_2$ in the troposphere. Similarly, losses of NH_3 and CH_3NH_2 by reaction with Criegee intermediates will be insignificant compared with reactions with OH radicals.

1. Introduction

Carbonyl oxides, or Criegee intermediates as they are commonly known, form during the ozonolysis of alkenes in the atmosphere.[1-4] These alkene ozonolysis reactions are exothermic and produce Criegee intermediates with a distribution of internal energies, some of which will be unstable to further decomposition. Collisions with the surrounding molecules in air can stabilize energized Criegee intermediates, and these species then undergo thermally activated unimolecular decomposition reactions or bimolecular reactions with H_2O, $(H_2O)_2$ and trace atmospheric species like SO_2, NO_2, alcohols and organic/inorganic acids.[5-10] The unimolecular reaction of the simplest and the most abundant Criegee intermediate, CH_2OO, is slow[11, 12] and the reaction with $(H_2O)_2$ is sufficiently fast to be the dominant loss mechanism in the troposphere.[13-15] Larger Criegee intermediates like $(CH_3)_2COO$ react slowly with H_2O and $(H_2O)_2$ and thus are consumed by reaction with trace atmospheric species in the troposphere, or competitive unimolecular loss.[16-19] The unimolecular reaction of methyl vinyl ketone oxide, a Criegee intermediate produced from ozonolysis of isoprene, and its reaction with water are thought to be sufficiently slow to sustain a large steady state concentration in equatorial regions.[9, 20, 21] The reactions of Criegee intermediates with SO_2 are fast and produce SO_3 which is a precursor for H_2SO_4 in the atmosphere.[4, 11, 16, 17, 22-24] Reactions with organic and inorganic acids occur with rate coefficients close to, or above the gas collision limit, and could be significant sinks for these acids in the troposphere.[8, 10, 25, 26] The functionalized organic hydroperoxide adducts thought to

[a] School of Chemistry, University of Bristol, Cantock's Close, Bristol BS8 1TS, UK Email: rcpchem@gmail.com.
[b] Max Planck Institute for Solid State Research, Heisenbergstraße 1, 70569 Stuttgart, Germany
[c] Combustion Research Facility, Mailstop 9055, Sandia National Laboratories, Livermore, California, 94551, USA
[d] College of Engineering, University of Georgia, Athens, GA 30602, USA
[e] Department of Chemistry, University of Georgia, Athens, GA 30602, USA
[f] Jet Propulsion Laboratory, California Institute of Technology, 4800 Oak Grove Drive, Pasadena, CA 91109, USA
[g] Mechanical Engineering, Stanford University, Stanford, CA 94305, USA
Electronic Supplementary Information (ESI) available: See DOI: 10.1039/x0xx00000x

Please do not adjust margins

form from Criegee intermediate reactions with organic acids and alcohols can condense to form secondary organic aerosols.[8, 9, 27]

Ammonia (NH_3) and amines are important trace atmospheric gases, with animal husbandry, nitrogen-fertilizer application, vegetation, ocean, biomass burning and fossil fuel combustion as some of their main sources.[28] NH_3 mixing ratio of up to 6 ppbv and amine mixing ratio of up to 10 pptv have been measured in remote and urban sites.[29] These compounds contribute to important atmospheric processes including aerosol nucleation and secondary organic aerosol formation.[28, 30, 31] The tropospheric concentration of amines is generally lower than that of ammonia by 2-3 orders of magnitude.[28, 32] However, amines can react with acids to form ammonium salts, leading to aerosol formation 25 to 100 times more effectively than for ammonia.[33] The sinks of NH_3 and amines in the troposphere include oxidation reactions initiated by OH radicals, gas-to-particle conversion, and surface deposition (both wet and dry).[34]

Jørgensen and Gross reported computational investigations of various Criegee intermediate reactions with NH_3, and suggested these reactions proceed by formation of a pre-reactive complex.[35] Schaefer and co-workers recently revisited these reactions, and reported rate coefficients obtained using quantum chemical calculations at a higher level of theory.[36] Both studies indicate that these reactions are not competitive with other reactions of Criegee intermediates, and may be important only in locations with intensive farming. In the current study, we present the first direct kinetic measurements for the $CH_2OO + NH_3$, $(CH_3)_2COO + NH_3$ and $CH_2OO + CH_3NH_2$ reactions, and product characterisation for $CH_2OO + NH_3$ and $CH_2OO + CH_3NH_2$ reactions. We explore the pressure and temperature dependence of the rates of these reactions, and interpret the outcomes with the aid of master equation modelling of the kinetics using electronic structure calculations of the key species along the reaction pathways.

2. Experimental

2.1. Cavity Ring-down Spectroscopy: The measurements of reaction rate coefficients used cavity ring-down spectroscopy (CRDS) to monitor changes in concentration of Criegee intermediates under different chemical and physical conditions. The lasers and the CRDS method used in this work have been described in detail previously.[11] In short, the 355-nm radiation used to probe Criegee intermediate concentrations by CRDS was generated by frequency doubling the 710-nm fundamental output from a dye laser pumped by the second harmonic of a Nd:YAG laser. The ring-down signals were detected by a photodiode and digitized using an oscilloscope. The chemistry in the flowing gas mixture was initiated by 355-nm UV pulses from the third harmonic of a Nd:YAG laser which crossed the probe laser axis at a shallow angle. The time delay between the photolysis and probe lasers was controlled by a digital pulse delay generator. A custom-written LabView virtual instrument was used to vary the time interval between photolysis and probe laser pulses, acquire and fit ring-down decay traces, and subtract background absorption contributions on the fly.

The CRD spectrometer was coupled with a temperature and pressure-controlled flow reactor, shown schematically in Figure S1 of Supplementary Information. Further details of the flow reactor were reported previously.[10] The middle part of the reactor was double jacketed, with the inner jacket containing circulated chiller fluid, and the outer jacket filled with an atmosphere of air for insulation. A Huber Unistat 360 dynamic temperature control system circulated the chiller fluid and controlled its temperature. The temperature range used for kinetic measurements was 240 – 320 K, with a maximum difference between the gas inlet and outlet ports of 2 K. The flow reactor temperature was stabilized for at least 30 minutes before taking measurements.

The *in-situ* production of Criegee intermediates used the method of Taatjes and co-workers of UV photolysis of an alkyl gem-diiodide in the presence of excess O_2.[16, 22] The flows of gas samples (N_2, O_2, alkyl diiodides and co-reactants NH_3 or CH_3NH_2) were regulated using calibrated mass flow controllers. A CH_2I_2 (99%) diiodide sample was obtained from Sigma Aldrich, whereas $(CH_3)_2CI_2$ was synthesized as described previously.[16] NH_3 (99.96%) and CH_3NH_2 (> 98%) gas samples were obtained from Argo International and Sigma-Aldrich, respectively. The degassed-diiodide, NH_3 and CH_3NH_2 samples were premixed with N_2 in glass bulbs before use.

2.2. Multiplexed Photo-Ionisation Mass Spectrometry: The reactions of carbonyl oxides with amines are predicted to form functionalized organic hydroperoxide association products.[35, 36] If these products absorb the UV wavelength used to probe CH_2OO in the CRDS measurements, the kinetics determinations could be adversely affected. Therefore, the reactions of formaldehyde oxide with NH_3 and CH_3NH_2 were also investigated at 298 K and 4 Torr using the Sandia multiplexed photoionization mass spectrometry (MPIMS) instrument interfaced with the tunable VUV-output of the Chemical Dynamics Beamline (9.0.2) at the Advanced Light Source, Lawrence Berkeley National Laboratory. This experiment has been described in detail elsewhere,[37] but is summarized briefly herein. Reagent (CH_2I_2, O_2), co-reactant (NH_3 or CH_3NH_2) and bath (He) gases were introduced via a set of calibrated mass flow controllers into a halocarbon wax-coated quartz reactor, held at 4 Torr via a feedback-controlled butterfly valve. The formaldehyde oxide Criegee Intermediate was photolytically generated using a 351-nm excimer laser aligned along the axis of the reactor.[22] Reactants and products were continuously sampled via a ~0.65 mm diameter orifice in the sidewall of the reactor, by which a molecular beam was generated. The molecular beam was orthogonally intercepted by the VUV ionizing radiation and the resultant ions were detected via orthogonal acceleration time of flight mass spectrometry.

2.3. Electronic Structure Calculations: Reaction pathways and photofragmentation for the various reactants and products were predicted using quantum chemistry calculations. Previous theoretical investigations confirmed that the $CH_2OO + NH_3$ reaction proceeds via a singlet electronic state with a simple single-reference character and that, at the basis set limit, the

coupled-cluster singles and doubles with perturbative triples (CCSD(T)) method provides a quantitatively accurate potential energy surface with an error range of less than 5 kJ/mol arising from higher-order correlation and non-adiabatic effects.[35, 36, 38] Geometries and harmonic frequencies of the stationary points for the complexation and subsequent reaction of CH_2OO with both NH_3 and CH_3NH_2 were therefore determined with the explicitly correlated CCSD(T)(F12*) method[39] using a cc-pVDZ-F12 basis set. At each of these geometries, CCSD(T)(F12*)/cc-pVQZ-F12 single-point energies were computed. An exponential correlation factor with length-scale 1.0 a_0 was used,[40] and core electrons were excluded from the correlation treatment. The coupled-cluster calculations were performed using the Molpro program.[41]

The appearance energies for various ionisation processes were computed at B3LYP/6-31+G(d) and CBS-QB3 levels of theory, and were corrected for the zero-point energies of the initial and final states. Adiabatic ionisation energies were calculated by taking the energy difference between the optimized cationic and neutral geometries. Fragmentation energies were obtained by taking the energy difference between the optimized transition state for the fragmentation process and the neutral geometries. Intrinsic reaction coordinate (IRC) calculations at a step size of 0.05 bohr were also performed at the B3LYP/6-31+G(d) level of theory, starting with the optimised transition state geometry for the fragmentation process. All the B3LYP/6-31+G(d) and CBS-QB3 calculations were performed using the Gaussian 09 program.[42]

2.4. Master Equation Kinetic Modelling: The microcanonical kinetic evolutions of the CH_2OO + NH_3 and CH_2OO + CH_3NH_2 reactions were studied using the open source master equation code MESMER.[43] The energy-grained master equation (EGME) was solved, wherein the internal (ro-vibrational) energy space of the reaction intermediates was partitioned into energy grains of a set size. The EGME approach then solved the coupled set of differential rate equations describing grain-to-grain transitions, which included both reactive transitions between different chemical species and transitions between the energy grains of a specific species by energy transfer with a system bath. The EGME approach used has been extensively documented previously.[44, 45]

The rigid rotor harmonic oscillator approximation was assumed, using the structures and vibrational frequencies from our electronic structure calculations. The barrier height was adjusted to fit the experimentally measured CH_2OO loss rates using a Levenberg-Marquardt algorithm. Collisional energy transfer was considered using an exponential-down model. The barrierless association reactions of CH_2OO with NH_3 and CH_3NH_2 were treated using an inverse Laplace transform.[46] In this treatment, a temperature independent capture rate coefficient of 1×10^{-10} molecule^{-1} cm^3 s^{-1} was used, which is consistent with the type of barrierless association considered. Preliminary calculations demonstrated that for both the reaction systems, the submerged inner transition state is the bottleneck to reaction, and the master equation results were insensitive to variations in the choice of ILT capture rate. Tunnelling was incorporated using an asymmetric Eckart potential parameterised by the imaginary frequency of the transition state (TS).

In all these calculations, the grain size used for the EGME calculations was 10 cm^{-1} and the average energy transfer upon collision ($\langle\Delta E_{down}\rangle$) parameter was assigned as 200 cm^{-1} for all wells. Initial tests showed the overall master equation rates were relatively insensitive to the energy transfer parameters compared to the barrier heights for the transition states. The MESMER input used in the current work is given in the Supplementary Information.

3. Results and Discussion

In this section, the outcomes of the experimental determinations of temperature and pressure dependent reaction kinetics are first presented. Reaction pathways are then accounted for using the results of photoionization and mass spectrometry studies, supported by electronic structure calculations of parent and fragment ion appearance energies. Finally, the kinetic data are quantitatively interpreted with the aid of master equation kinetic modelling. Discussion of atmospheric implications is deferred to Section 4.

3.1 Reaction Kinetics: Rate coefficients k_1, k_2 and k_3 were determined for the respective reactions of CH_2OO with NH_3 and CH_3NH_2, (R1) and (R2), and $(CH_3)_2COO$ with NH_3 (R3) using CRDS. The measurements were performed over a temperature range from 240 – 320 K, which is significant for the tropospheric boundary layer, and at pressures from 10 – 100 Torr.

$$CH_2OO + NH_3 \rightarrow \text{Products} \qquad \text{(R1)}$$

$$CH_2OO + CH_3NH_2 \rightarrow \text{Products} \qquad \text{(R2)}$$

$$(CH_3)_2COO + NH_3 \rightarrow \text{Products} \qquad \text{(R3)}$$

Figure 1 shows an example plot of the decays of CH_2OO absorption, measured as a change in ring-down rate coefficient $\Delta\kappa$, in the presence of various concentrations of NH_3 at 10 Torr total pressure and 248 K. Excess NH_3 was used, such that the CH_2OO + NH_3 reaction is in the pseudo first-order regime. Contributions remain from the fast self-reaction of the Criegee intermediate,[11] hence the decay of CH_2OO in the presence of NH_3 exhibited simultaneous first and second order behaviour. The CRDS measurements were therefore fitted using an integrated rate expression:

$$\Delta\kappa(t) = \frac{k_p}{\frac{k_p}{\Delta\kappa(t_0)}e^{k_p t} - k'\left(\frac{2L}{cd}\right) + k'\left(\frac{2L}{cd}\right)e^{k_p t}} \qquad \text{(E1)}$$

Here, $\Delta\kappa(t)$ is the change in the ring-down rate caused by the photolysis laser at different time delays, t, between the photolysis and probe lasers, k_p accounts for the pseudo first-order loss rate coefficient for bimolecular reaction of the Criegee intermediate with excess ammonia (R1) and thermal decomposition, L = 106 cm is the ring-down cavity length, d = 7.6 cm is the laser overlap length, $k' = k_{obs}/\sigma_{355nm}$ is the effective second-order self-reaction loss rate coefficient of the Criegee intermediate scaled by its absorption cross section at

the probe laser wavelength, and c is the speed of light. A detailed derivation of equation (E1) is provided elsewhere.[11] At each experimental temperature and pressure, kinetic fitting was performed for Criegee intermediate decay traces obtained in the absence of co-reactants by varying the parameters $k', \Delta\kappa(t_0)$ and k_p (to allow for unimolecular decomposition). The k' value thus obtained was constrained in the kinetic fits to obtain k_p values from Criegee intermediate decay traces obtained in the presence of excess co-reactant at the same temperature and pressure. The slope of a linear fit to the variation of k_p with co-reactant NH_3 concentration shown in the inset of Figure 1 gives the rate coefficient for the bimolecular reaction (R1). The intercept of the linear fit is a sum of contributions from the Criegee intermediate unimolecular loss and reactions with other species like peroxy radicals and iodine atom in the flow reactor.[11]

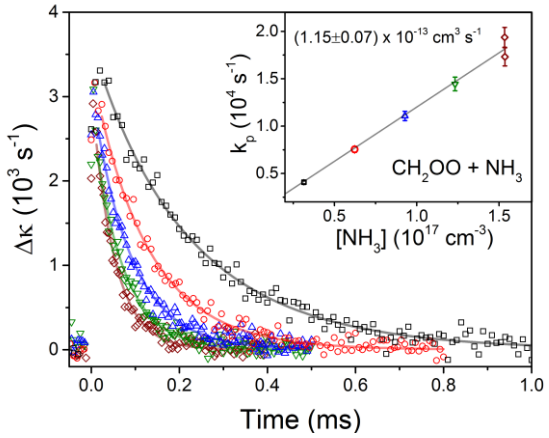

Figure 1: Representative example of a bimolecular reaction rate coefficient measurement. The main plot shows decays of the CH_2OO absorption, represented as changes in ring-down rate coefficients, in the presence of various concentrations of NH_3 at 10 Torr total pressure and a temperature of 248 ± 2 K. The solid lines show fits obtained using the simultaneous first and second-order function of equation (E1). The inset shows the pseudo first-order rate coefficients obtained from the fits for different NH_3 concentrations. The gradient of a linear fit gives the bimolecular rate coefficient for the $CH_2OO + NH_3$ reaction at 248 ± 2 K. The highest and lowest concentration measurements were repeated to ensure reproducibility.

The rate coefficients k_1 and k_2 for the reactions of CH_2OO with NH_3 and CH_3NH_2 were measured as a function of total pressure, as shown in Figure 2. The total pressure in the reactor was raised by increasing the flow of N_2 bath gas. Both k_1 and k_2 values were found to be independent of pressure within the 10 to 100 Torr range, and an average value with 2σ uncertainty provides the best estimates of $k_1 = (8.4 \pm 1.2) \times 10^{-14}$ cm^3 s^{-1} and $k_2 = (5.6 \pm 0.4) \times 10^{-12}$ cm^3 s^{-1} at 293 K. The former value is in good agreement with a recent report of $k_1 = (8.1 \pm 1.0) \times 10^{-14}$ cm^3 s^{-1} at 100 Torr and 298 K by Yang and co-workers using a direct UV absorption spectroscopy method.[47] Figure S2 of the Supplementary Information shows the decay traces of $(CH_3)_2COO$ in the presence of various concentrations of NH_3, and Figure S3 shows the pseudo first order rate coefficients obtained from these traces. These measured rate coefficients are of similar magnitude to the unimolecular decay rate coefficient of $(CH_3)_2COO$. Thus, only an upper limit of $k_3 \leq 2.7 \times 10^{-15}$ cm^3 s^{-1} can be estimated. Figure 3 shows the k_1 and k_2 values obtained in the 240 to 320 K temperature range. The $k_2(T)$ values measured at 10 and 50 Torr total pressures are in good agreement, further confirming the weak pressure dependence of these reactions over the range studied. The k_1(p,T) and k_2(p,T) values are provided in the Tables S1 and S2 in the supplementary information.

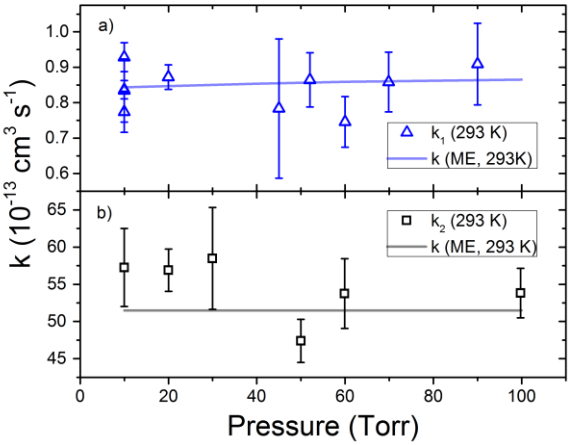

Figure 2: Pressure dependence of the rate coefficients for: a) $CH_2OO + NH_3$ (k_1); and b) $CH_2OO + CH_3NH_2$ (k_2) reactions. All the measurements were made at a fixed temperature of 293 K. The solid lines show master equation fits, details for which are provided in the text.

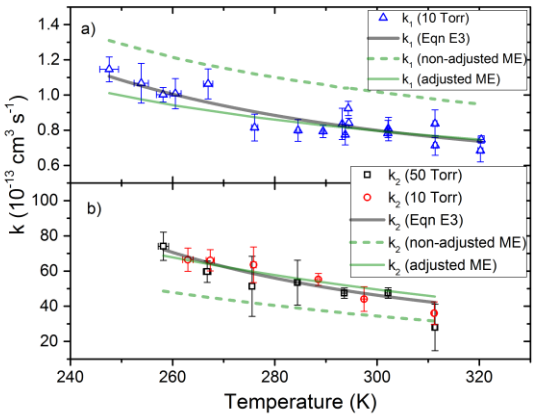

Figure 3: Temperature dependence of the rate coefficients for the reactions of: a) $CH_2OO + NH_3$ (k_1); and b) $CH_2OO + CH_3NH_2$ (k_2). The k_1 values were obtained at a total pressure of 10 Torr, whereas k_2 values were measured at total pressures of 10 and 50 Torr (see inset key). The black solid lines show fits obtained using equation (E3), derived assuming the steady state approximation. The green dashed and solid lines show fits obtained using a master equation treatment with *ab initio* and adjusted barrier heights (see main text). The master equation

fits are from 10 Torr simulations, although negligible pressure dependence is observed in the experimental data.

3.2. Product Characterisation: Complementary experiments were performed using MPIMS at the ALS for reactions of CH_2OO with NH_3 and CH_3NH_2. CH_2OO decay traces were measured at a photoionization energy of 10.5 eV, in the presence of either CH_3NH_2 or NH_3 as shown in Figure S4 to obtain bimolecular reaction rate coefficients. For the CH_2OO + NH_3 reaction, the signal-to-noise levels were insufficient for reliable kinetic analysis. Figure S5 shows the bimolecular plot for dependence of CH_2OO decay rate coefficients on CH_3NH_2 concentration. A bimolecular rate coefficient value of $(4.3 \pm 0.5) \times 10^{-12}$ cm^3 s^{-1} is obtained at 298 K and 4 Torr He, in good agreement with the CRDS measurement of $(4.4 \pm 0.7) \times 10^{-12}$ cm^3 s^{-1} at 297.5 K and 10 Torr N_2. This comparison indicates that the absorbance of the product at the probe wavelength makes a relatively small contribution to the kinetic decay profiles obtained using CRDS.

For both NH_3 and CH_3NH_2 reactions, products were not observed at the parent mass of the functionalized organic hydroperoxides. However, daughter ions were observed at exact masses consistent with fragment ions produced via loss of HO_2, H_2O and NH_2 from the hydroperoxide product. Dissociative ionization of organic hydroperoxides has previously been observed for the products of Criegee Intermediate reactions with organic acids.[8] For the CH_2OO + NH_3 reaction (Figure S4), signal at m/z 47 (CH_2OOH^+) is observed, which is consistent with the fragment ions observed from functionalized organic hydroperoxides formed via Criegee Intermediate + organic acid reactions. For the CH_3NH_2 reaction, the formation rates of the daughter ions at m/z 44, 953 ± 124 s^{-1}, and m/z 59, 804 ± 195 s^{-1}, agree with the loss rate of m/z 46, 782 ± 78 s^{-1} (Figure 4, inset). The m/z 46 is assigned to Criegee intermediate CH_2OO based on previous observations.[8, 22] The amplitudes of the m/z 44 (Figure S6a) and m/z 59 (Figure S6b) fragments are observed to scale with increasing CH_3NH_2 concentration and are not observed in the absence of CH_3NH_2. Figure 4 shows the photoionization spectra for m/z 46, 44 and 59 cations, obtained by integrating the kinetic time profiles in the 9.5 to 11.5 eV energy range and the appearance energies are provided in Table 1. The m/z 46 cation signal is significantly lower than the other two cations because of its rapid reactive loss. The appearance energy for the m/z 44 cation was estimated by linear extrapolation of the ion signal in the 9.5 to 10 eV range.

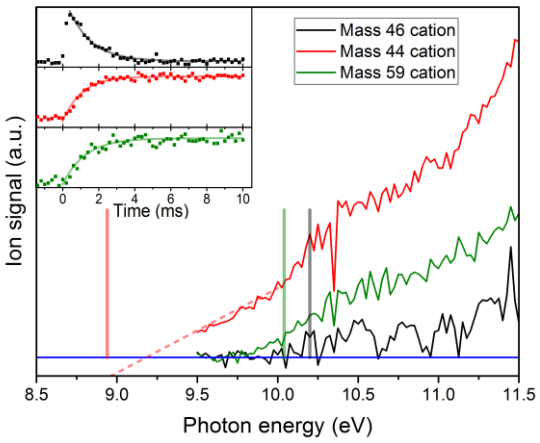

Figure 4: Photoionization spectra for m/z 44, 46 and 59 cations from the CH_2OO + CH_3NH_2 reaction (298 K, 4 Torr He). The spectra were obtained by integrating cation signals over the kinetic timescales at each photon energy. The red dashed line shows an extrapolated linear fit to the m/z 44 ion signal in the 9.5 to 10 eV range. The blue line represents zero signal. The solid vertical lines denote calculated appearance energies at the CBS-QB3 level of theory, listed in Table 1. The inset shows temporal profiles of the various cations obtained by integrating the ion signals in the 9.5 to 11.5 eV range. The solid lines in the inset are kinetic fits to the temporal profiles.

Table 1: Appearance energies of various cations produced from photoionization of the functionalized organic hydroperoxide produced from CH_2OO reaction with CH_3NH_2. The calculations were performed at the B3LYP/cc-pVTZ and CBS-QB3 levels of theory and details are provided in the text. The structures of the cations are shown in Figure 5.

Photoionization Process	Appearance Energy (eV)		
	Experimental	B3LYP/ cc-pVTZ	CBS-QB3
$CH_3N(H)CH_2OOH \rightarrow CH_3N(H)CH_2OOH^+$		8.38	8.75
$CH_3N(H)CH_2OOH \rightarrow CH_3N(H)CH_2^+ + HO_2$	9.2 (m/z 44)	8.50	8.94
$CH_3N(H)CH_2OOH \rightarrow CH_3N(H)CHO^+ + H_2O$	9.8 (m/z 59)	9.75	10.04

To characterize the observed mass fragments, the appearance energies were calculated for various photoionization pathways using B3LYP/cc-pVTZ and CBS-QB3 methods, with the outcomes shown in Table 1. The appearance energy for ionization of the proposed hydroperoxide product to its cation (the adiabatic ionization energy) is lower than the observed appearance energies of the m/z 44 and 59 cations, consistent with fragmentation of the hydroperoxide cation. The appearance energies were also calculated for various fragmentation processes by taking the energy difference between the transition state for the cation fragmentation and the neutral adduct, and are in good agreement with the observed appearance energy values. The appearance energy of the m/z

44 cation is consistent with fragmentation of the hydroperoxide cation to HO_2 and a $CH_3N(H)CH_2^+$ cation, while the appearance energy of the m/z 59 cation conforms with fragmentation of the hydroperoxide cation to H_2O and $CH_3N(H)CHO^+$ cation. The transition states for fragmentation of the hydroperoxide cation were optimized and verified to have one imaginary frequency. Intrinsic reaction coordinate calculations were also performed for the two fragmentation processes at the B3LYP/6-31+G(d) level of theory, and the results are shown in Figure 5. The fragmentation process to mass 59 is exothermic with a calculated excess energy of ~3.5 eV, whereas the fragmentation to mass 44 is nearly isoenergetic, with a calculated excess energy of ~0.2 eV. Overall, the MPIMS observations are consistent with production of a functionalized organic hydroperoxide adduct $CH_3N(H)CH_2OOH$ from the CH_2OO + CH_3NH_2 reaction.

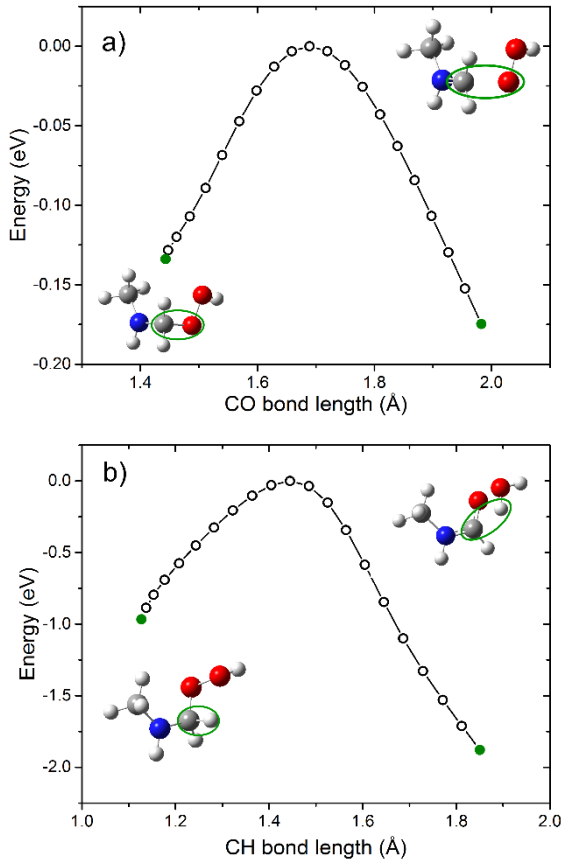

Figure 5: Intrinsic reaction coordinates for fragmentation of a $CH_3N(H)CH_2OOH^+$ hydroperoxide cation to a) $CH_3N(H)CH_2^+$ + HO_2 and b) $CH_3N(H)CHO^+$ + H_2O, calculated at the B3LYP/6-31+G(d) level of theory. The abscissae show the changes in the lengths of the C-O or C-H bonds ringed in green and involved in the fragmentation mechanism, projected from the IRC calculated geometries. Computed molecular structures are shown for the reactants and products.

3.3. Macroscopic Steady State Kinetic Modelling: As Figure 3 shows, the k_1 values increase with a decrease in temperature, which is consistent with the computed formation of a pre-reactive complex leading to a TS for insertion of the CH_2OO into an N-H bond.[35, 36] For the purpose of a steady-state kinetic analysis, we model the reaction using the following scheme with reversible complex formation:

$$CH_2OO + NH_3 \rightleftarrows \text{Complex} \qquad \text{(R4)}$$

$$\text{Complex} \rightarrow \text{Product} \qquad \text{(R5)}$$

The predicted temperature dependence of the overall reaction rate coefficient (k_r), obtained by applying the steady-state approximation to the concentration of the pre-reactive complex, is given by:

$$k_r = \frac{k_4}{k_{-4}} k_5 = K_{eq} k_5 \qquad \text{(E2)}$$

Using statistical thermodynamics and TST, equation E2 can be approximated as:

$$k_r = AT^2 exp\left(-\frac{\Delta H}{RT}\right) \qquad \text{(E3)}$$

Here, A and ΔH are treated as temperature-independent, and are given by:

$$A = \frac{R' k_B}{N_A h} exp\left(\frac{\Delta S_4 + \Delta S_5}{R}\right) \qquad \text{(E4)}$$

$$\Delta H = \Delta H_4 + \Delta H_5 \qquad \text{(E5)}$$

In Equations (E3 – E5), $R'$and R denote the molar gas constant in different units (R' =82.1 cm^3 atm mol^{-1} K^{-1} and R = 8.31 J mol^{-1} K^{-1}), N_A is the Avogadro constant, k_B is the Boltzmann constant, and T is the absolute temperature. ΔS_5 and ΔH_5 are the entropy and enthalpy changes for activation of the pre-reactive complex to the TS for product formation via reaction (R5). ΔS_4 and ΔH_4 are the changes in entropy and enthalpy for the complexation step, (R4). A derivation of equation (E3) is provided in our previous study.[10] Figure 3 includes fits to the experimental $k_1(T)$ and $k_2(T)$ values obtained with equation (E3). The quality of both fits is good, with adjusted R^2 values greater than 0.8, and Table 2 summarizes the values of the parameters obtained. The derived ΔH values are negative for both reactions, showing that the reactions have a submerged barrier with a barrier height that decreases with methyl substitution on the ammonia. The ΔS_5 value for formation of a cyclic TS from the pre-reactive complex is expected to be smaller than the ΔS_4 value for complexation of two separated species. Thus, the negative $\Delta S = \Delta S_4 + \Delta S_5$ values obtained for both reactions indicate the loss in entropy from complexation.

Table 2: Values of the parameters A, ΔS, and ΔH obtained from the fits to Equation (E3) shown in Figure 3. The fit parameters are defined in the main text.

Reaction	A ($cm^3\ s^{-1}\ K^{-2}$)	ΔS ($J\ mol^{-1}\ K^{-1}$)	ΔH ($kJ\ mol^{-1}$)
$CH_2OO + NH_3$	$(3.1 \pm 0.5) \times 10^{-20}$	-152^{+2}_{-1}	-8.4 ± 0.4
$CH_2OO + CH_3NH_2$	$(5 \pm 2) \times 10^{-19}$	-129^{+4}_{-3}	-11.5 ± 0.8

3.4. Reaction Pathway Calculations: The CCSD(T)(F12*) reaction profiles for CH_2OO with NH_3 and CH_3NH_2 are displayed in Figure 6. In both cases, there is a shallow potential energy minimum corresponding to a pre-reactive, hydrogen-bonded complex of the amine at the external oxygen site, with the H-bond partially disrupting the π-system. For $CH_2OO + CH_3NH_2$ the computed barrier to subsequent reaction is submerged, at -20.7 kJ mol^{-1}, in qualitative agreement with an experimentally derived activation barrier of -11.5 kJ mol^{-1} obtained using steady-state kinetic analysis (see Section 3.3). For the $CH_2OO + NH_3$ reaction, the situation is more complicated. Although our basis-set-limit CCSD(T) barrier is submerged, at -2.7 kJ mol^{-1}, applying the higher-order corrections computed by Schaefer and co-workers raises our calculated barrier to +1.1 kJ mol^{-1} above the reactants.[36] Using their computed barrier of +1.8 kJ mol^{-1}, transition state theory (TST) and the steady-state approximation, Schaefer and co-workers predicted a rate coefficient at 298 K of $k_1 = 5.36 \times 10^{-14}\ cm^3\ s^{-1}$, which is a factor of two smaller than our experimental value. Accounting for the missing anharmonic contributions to the zero-point energy would likely submerge the barrier, which would increase the predicted rate coefficient. The application of canonical TST assumes the pre-reaction complex to be in a steady state and thermalized, and these assumptions are explored here. The calculated energy values for $CH_2OO + NH_3$ and $CH_2OO + CH_3NH_2$ reactions are provided in the Tables S3 and S4 in the supplementary information.

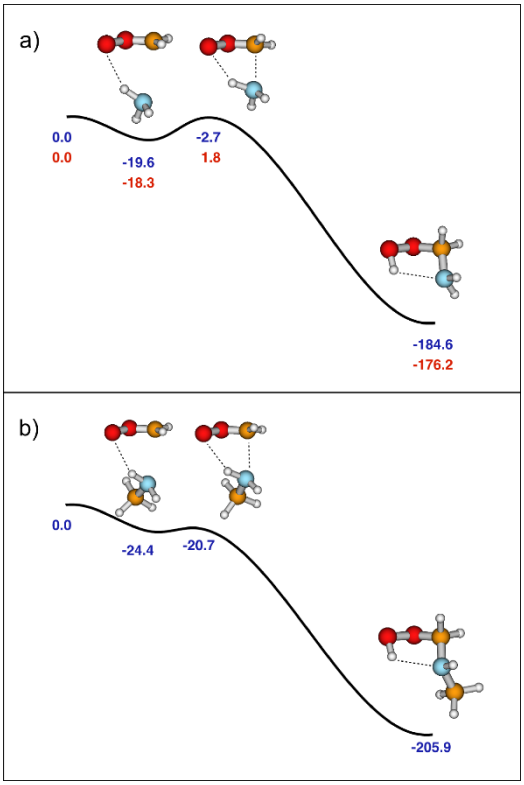

Figure 6: Reaction profiles for a) CH_2OO+NH_3 and b) $CH_2OO + CH_3NH_2$ with energies specified in kJ mol^{-1}. Energies were calculated at the CCSD(T)(F12*)/cc-pVQZ-F12//CCSD(T)(F12*)/cc-pVDZ-F12 level of theory and are given in blue. Focal point energies from Schaefer and co-workers are given in red.[36]

3.5. Master Equation Kinetic Modelling: A micro-canonical description of the kinetics in the form of the master equation (ME) goes beyond the steady-state approximation and does not assume that the pre-reactive complex is stabilised with a thermalized energy distribution. This ME treatment allows us to examine the applicability of the steady-state treatment coupled with the canonical treatment used by Misiewicz *et al.* and Jørgensen *et al.* for the $CH_2OO + NH_3$ reaction.[35, 36] We used rigid rotor and harmonic energy levels provided by basis-set-limit CCSD(T) theory, but adjusted the barrier to fit the experimental rate coefficients. The top panel of Figure 3 compares the experimental, theoretical (with ab initio barrier) and barrier-adjusted theoretical rate coefficients for the $CH_2OO + NH_3$ system and displays good agreement. The fitted barrier was determined to be -2.1 ± 0.1 kJ mol^{-1}, within the anticipated error bar of both the current high-level calculations and the previous work of Misiewicz *et al.* The quoted uncertainty is the 2σ value of the fit. Similar calculations were performed for the reaction between CH_2OO and CH_3NH_2, and again the TS energy was varied to fit the experimental data. These simulations demonstrate that, despite being submerged, this TS structure is still sufficiently tight to form a kinetic bottleneck. The fitting calculations return an energy of -22.4 ± 0.2 kJ mol^{-1} with respect to the reactants. A comparison between computed and experimental rate coefficients is shown in Figure 3(b), and again

displays good agreement. The fitted values for $CH_2OO + NH_3$ and $CH_2OO + CH_3NH_2$ reactions are provided in Tables S5 and S6 in the supplementary information.

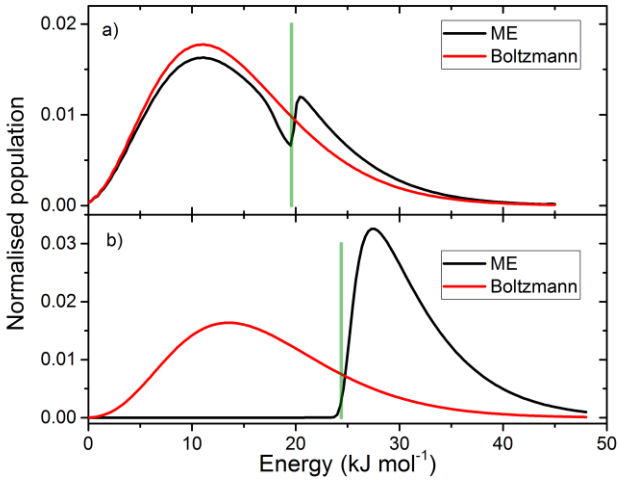

Figure 7: Steady state energy distributions (black lines) for the pre-reaction complex for: a) the $CH_2OO + NH_3$; and b) the $CH_2OO + CH_3NH_2$ reactions, taken from the master-equation (ME) simulations. In both cases these distributions are taken after 0.1s reaction time and are compared with the Boltzmann distribution (red line) for the same complex. These simulations were performed at 293 K and 10 Torr of N_2 bath gas. The vertical green lines show the binding energies of the pre-reaction complexes.

From the ME simulations, it was also possible to test the steady state assumption used by Misiewicz *et al.* and Jørgensen *et al.*[35, 36] The MESMER calculations track the time evolution of each energy grain in the reactive system, from which the distribution of internal energies in the pre–reaction complex may be obtained at any point in the reaction. In both systems studied here, a steady distribution of energies is established on the 10^{-6} s timescale or faster, and Figure 7 compares these steady distributions to the Boltzmann distribution. From this figure it is evident that the complex cannot be considered thermalized and the factors affecting the shape of the distributions are as follows. For both systems, the pre-reaction complex is formed via reaction R4 and then rapidly dissociates back to reactants (R-4) reaching a microcanonical equilibrium between reactants and complex. This equilibrium strongly favours the reactants such that at any given time the complex population will be many orders of magnitude lower than that of the reactants. This transient complex population may then undergo collisional activation or deactivation (k_{ET}) or react to products (R5). In the $CH_2OO + CH_3NH_2$ reaction, energy transfer is negligible relative to reaction (R5) because of the low reaction barrier, as shown in Figure 6(b). Thus, at any given time the energy distribution in the transient complex population is unperturbed from the nascent energy distribution in the pre-reaction complex as seen in Figure 7(b).

In the case of the $CH_2OO + NH_3$ reaction, the transition state for reaction (R5) is close to the reactant energy, as shown in Figure 6, which results in a much slower microcanonical rate coefficient compared to the $CH_2OO + CH_3NH_2$ reaction. Competitive collisional stabilization thus occurs for some fraction of the transient pre-reactive complex. Figure 8 presents a schematic representation of the competition between collisional stabilization and reaction, in which different regions of behaviour are identified. The complex initially forms with a nascent energy distribution closely related to that of the reactants (Region 1). If the complex is stabilised to energies below that of the reactants (region 2), the microcanonical rate coefficients k(E) for reactions (R4) and (R-4) become zero, whereas k(E) values for R5 remain large because of the submerged TS. Thus, the loss of the complex by R5 is efficient, but the population is only replenished by rare collisional deactivation from higher energies, leading to a lower steady-state concentration in this energy region compared to the higher energy region. Finally, some fraction of the complex in region 3 (Figure 8) is stabilised further due to the predominance of collision events, forming a second Boltzmann-like peak in population at low energies. All these competing processes rapidly form the bimodal distribution of energies in the pre-reaction complex population for the $CH_2OO + NH_3$ reaction, as is shown in Figure 7(a).

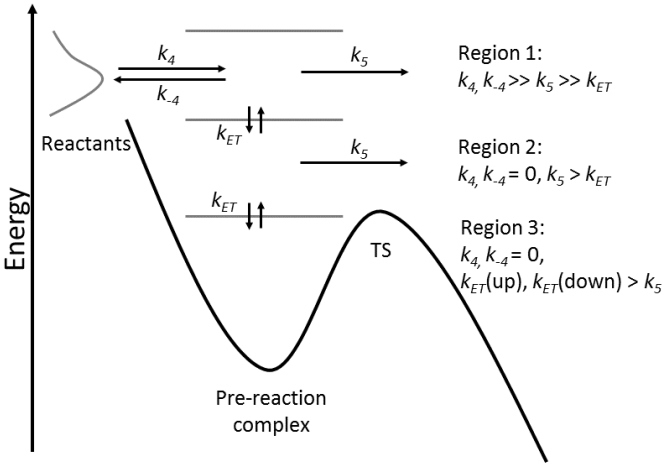

Figure 8: Schematic diagram showing the competing complexation and reactive processes involved in the $CH_2OO + NH_3$ and $CH_2OO + CH_3NH_2$ reactions. Three regions are classified based on the rate coefficient magnitudes for these processes, and are described in the text.

The ME analysis shows that there are two main assumptions in the macroscopic steady-state kinetic modelling which are of questionable validity: (1) the steady state approach uses high pressure limiting rate coefficients, but the ME analysis shows k_4, k_{-4} and k_5 to be well into the fall-off curve; (2) the ME distributions are non-Boltzmann, as shown in Figure 7, and thus macroscopic rate coefficients originating from the complex are ill-defined. Hence, the ΔH values shown in Table 2 only provide a qualitative measure for the reaction barrier height, and a full microcanonical treatment is necessary. Tables S5 and S6 compare rate coefficient values obtained from the full ME treatment, k_{ME}, and from the steady state approximation coupled with canonical rate coefficients, k_{CAN}. The canonical

rate coefficients for the reactions (R4), (R-4) and (R5) were obtained from the optimized master equation model using MESMER. The k_{CAN} values were found to be significantly higher than k_{ME} value for the $CH_2OO + CH_3NH_2$ reaction as the k_{-4} and k_5 values are of similar magnitude and the canonical steady state approximation is not valid. For the $CH_2OO + NH_3$ reaction, the k_{CAN} value is much closer but still systematically higher compared to the k_{ME} values, supporting the need for a full ME treatment.

The ME simulations allow a rationalization of the negative temperature dependence observed in the rate coefficients for reactions (R1) and (R2). For reaction (R2), the ME distributions show that the reaction is prompt, with little or no stabilisation of the complex prior to product formation. If stabilisation of the complex is discounted, then the overall reaction rate is controlled by the competition between reactions (R-4) and (R5). Microcanonically (since the complex is non-Boltzmann), $k_{-4}(E)$ is found to reduce more rapidly with lower energies than $k_5(E)$ because of the submerged TS. Therefore, as the temperature decreases and the peak of the prompt energy distribution in the complex shifts to lower energies, the competition between reactions (R-4) and (R5) increasingly favours (R5). These same arguments also apply to reaction (R1), along with partial stabilisation of the complex. Analogous behaviour has been described in detail previously.[48, 49]

Our simulations confirm that the reactions of CH_2OO with NH_3 and CH_3NH_2 proceed via a pre-reactive complex with a submerged (or near energy neutral) barrier to product formation, leading to negative temperature dependence of the rate coefficient. The master-equation analysis also supports the experimental measurements in demonstrating that there is little pressure dependence to the observed rate coefficients under the conditions used here. The ME analysis provides a detailed description of the system, combining high level quantum chemistry calculations with experimental measurements. In contrast, the macroscopic steady state kinetic analysis provides a semi-empirical description of the reaction system with simple analytical expressions for the temperature dependence of the rate coefficients. For the slower reaction of $(CH_3)_2COO$ with NH_3, the prediction by Jørgensen and Gross of $k_3 = 5.1 \times 10^{-18}$ cm^3 s^{-1}, made using the G3 method for electronic structures and TST for the kinetics, is consistent with our upper-limit estimate.[35]

4. Atmospheric Implications

The main gas-phase chemical sinks for NH_3 and CH_3NH_2 in the troposphere are their reactions with OH radicals, with respective rate coefficients of 1.6×10^{-13} and 1.7×10^{-11} cm^3 s^{-1} at 298 K.[50, 51] In comparison, the rate coefficients for the CH_2OO reactions with NH_3 and CH_3NH_2 at 293 K are $k_1 = 8 \times 10^{-14}$ and $k_2 = 5.6 \times 10^{-12}$ cm^3 s^{-1}, respectively. The rate coefficient $k_3 \leq 2.7 \times 10^{-15}$ cm^3 s^{-1} for the reaction of $(CH_3)_2COO$ with NH_3 is significantly smaller than that for CH_2OO. The daytime OH radical steady state concentration is ~10^6 molecule cm^{-3},[52] which is greater than the highest predicted Criegee intermediate steady state tropospheric concentration of ~10^5 cm^{-3} in the forested equatorial regions.[9, 21, 53] Thus, considering the balance of concentrations and rate coefficients, the reactions of NH_3 and CH_3NH_2 with OH radicals should significantly outweigh those with Criegee intermediates in the troposphere as summarized in Table 3. In this analysis, all the Criegee intermediates were assumed to react with the same rate coefficient as CH_2OO, which is likely to be an overestimate because methyl substitution of the simplest Criegee intermediate significantly reduces its reaction rate coefficient with NH_3.

Table 3: Comparison of tropospheric loss processes for NH_3 and CH_3NH_2. The lifetime values τ_{OH} and τ_{CI} with respect to reaction with OH and Criegee intermediates were calculated assuming [OH] = 10^6 cm^{-3} and [CI] = 10^5 cm^{-3}, with CI denoting all Criegee intermediates.

	τ_{OH} (days)	τ_{CI} (days)	τ_{CI}/τ_{OH}
NH_3	72	1447	20
CH_3NH_2	0.7	21	30

The reactions of Criegee intermediates with NH_3 and CH_3NH_2 proceed with pre-reactive complex formation and through a five-membered cyclic transition state in which the terminal oxygen and carbonyl carbon of the Criegee intermediate approach the hydrogen and nitrogen of the NH_3 or CH_3NH_2, respectively, to produce functionalized organic hydroperoxides. Reactions of Criegee intermediate with H_2O,[12, 54, 55] H_2S[56, 57] and CH_3OH[9, 27] have been shown to proceed in a similar fashion. Figure 9 compares the rate coefficients of these reactions to the energies required to break the X-H bonds (X= S, O, N) in various co-reactants (H-SH, H-OCH_3, H-NH_2 and H-OH). The adjusted R^2 value for a linear fit is greater than 0.96, suggesting that these reactions have similar kinetic bottlenecks. Reactions of Criegee intermediates with carboxylic acids and nitric acid have also been shown to produce functionalized organic hydroperoxides.[8, 26] However, the transition states are significantly stabilised by formation of a seven-member cyclic structure which results in rate coefficient values in the range of 10^{-10} cm^3 s^{-1}, limited by the initial capture process. The five-membered cyclic transition states involved in Criegee intermediate reactions with H_2O are modified by the presence of another H_2O molecule to a seven-membered cyclic structure, similar to the acid reaction, which results in an almost four orders of magnitude increase in the rate coefficient.[55] Recently, the reaction of syn-CH_3CHOO with CH_3OH has been shown to be enhanced by up to a factor of 3 in the presence of a single water molecule because of similar stabilisation of the transition state.[58] The presence of H_2O may therefore stabilize the transition states involved in the reactions of Criegee intermediates with NH_3 and CH_3NH_2, resulting in larger rate coefficients under atmospheric conditions. The full atmospheric implications of these reactions will then depend on the propensities of atmospheric ammonia and amines to complex with water.

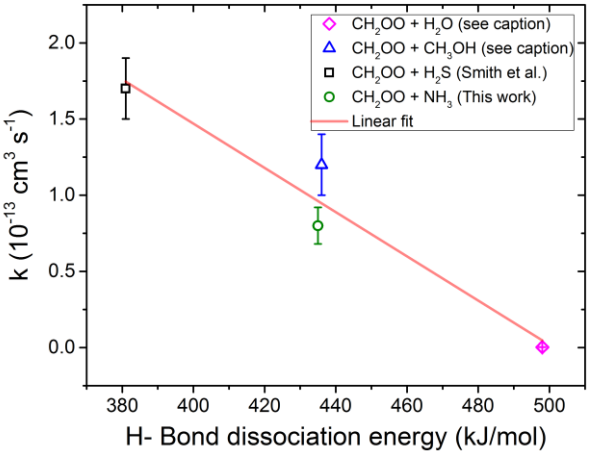

Figure 9: The dependence of rate coefficients for various reactions of CH_2OO Criegee intermediate on the bond dissociation energies for the labile hydrogen of the co-reactants. The rate coefficient for $CH_2OO + CH_3OH$ was obtained by averaging the values reported by McGillen et al.[9] and Tadayon et al.[27] The rate coefficient for $CH_2OO + H_2O$ was obtained by averaging the values reported by Berndt et al.[12] and Sheps et al.[15] The bond dissociation energies were obtained from Ref [59]. The red line is a linear fit without error weighting.

6. Conclusions

Bimolecular rate coefficients for the reactive removal of CH_2OO by NH_3 and CH_3NH_2, and of $(CH_3)_2COO$ by NH_3 are reported for a range of temperatures (240 – 320 K) and pressures (10 – 100 Torr). The 293 K rate coefficient for the $CH_2OO + NH_3$ reaction lies between, and is in reasonable agreement with, two prior theoretical predictions.[35, 36] The $CH_2OO + CH_3NH_2$ reaction is shown to produce $CH_3N(H)CH_2OOH$, a functionalized organic hydroperoxide. The observed pressure and temperature dependences are accounted for by a reaction mechanism, validated by master equation kinetic modelling, in which formation of a weakly bound pre-reaction complex of the Criegee intermediate and ammonia or methylamine precedes H-atom transfer via a tight transition state. In the $CH_2OO + NH_3$ and $CH_2OO + CH_3NH_2$ reactions, this activation barrier is deduced to lie lower in energy than the separated reactants. The different heights of the activation barriers control the overall reaction rate coefficients, with the $CH_2OO + CH_3NH_2$ reaction being the fastest of the three studied. None of the reactions are considered fast enough to compete with OH radical initiated removal of NH_3 and CH_3NH_2 in the Earth's troposphere, unless the rates are significantly enhanced by complexation with water molecules.

Conflicts of interest

There are no conflicts to declare.

Acknowledgements

Financial support for the University of Bristol group was provided by the Natural Environment Research Council (NERC) grants NE/K004905/1 and NE/P013104/1. MRM acknowledges supported by Marie Skłodowska-Curie Individual Fellowship HOMER (702794). RJS is supported by the US Air Force Office of Scientific Research (AFOSR) under Contract No. FA9550-16-1-0051. We thank Prof G.C. Lloyd-Jones and Drs C. Nottingham and T. West (University of Edinburgh) for the 2,2-diiodopropane sample. The participation of CJP is supported by the Jet Propulsion Laboratory, California Institute of Technology, under contract with the National Aeronautics and Space Administration (NASA), supported by the Upper Atmosphere Research and Tropospheric Chemistry programs. The participation of RLC, IOA, BR, KR, DLO, CAT and the development and operation of the MPIMS kinetics machine are supported by the Office of Chemical Sciences, Geosciences, and Biosciences, Office of Basic Energy Sciences, United States Department of Energy. Sandia National Laboratories is a multimission laboratory managed and operated by National Technology and Engineering Solutions of Sandia, LLC., a wholly owned subsidiary of Honeywell International, Inc., for the U.S. Department of Energy's National Nuclear Security Administration under contract DE-NA0003525. The Advanced Light Source is supported by the Director, Office of Science, Office of Basic Energy Sciences, U.S. Department of Energy under contract no. DE-AC02-05CH11231. This paper describes objective technical results and analysis. Any subjective views or opinions that might be expressed in the paper do not necessarily represent the views of the USDOE or the United States Government.

All experimental data are archived in the University of Bristol's Research Data Storage Facility:
DOI: 10.5523/bris.3lfkl8guhfjf2ain57w18p7ue

References

1. R. Criegee, Angew. Chem. Int. Ed., 1975, 14, 745-752.
2. J. G. Calvert, R. Atkinson, J. A. Kerr, S. Madronich, G. K. Moortgat, T. J. Wallington and G. Yarwood, The Mechanism of Atmospheric Oxidation of the Alkenes, Oxford University Press, New York, USA, 2000.
3. D. Johnson and G. Martson, Chem. Soc. Rev., 2008, 37, 699-716.
4. C. A. Taatjes, D. E. Shallcross and C. J. Percival, Phys. Chem. Chem. Phys., 2014, 16, 1704-1718.
5. C. A. Taatjes, Annu. Rev. Phys. Chem. , 2017, 68, 183-207.
6. J. J.-M. Lin and W. Chao, Chem. Soc. Rev., 2017, 46, 7483-7497.
7. M. A. H. Khan, C. J. Percival, R. L. Caravan, C. A. Taatjes and D. E. Shallcross, Environ. Sci: Processes Impacts, 2018, 20, 437-453.
8. R. Chhantyal-Pun, B. Rotavera, M. R. McGillen, M. A. H. Khan, A. J. Eskola, R. L. Caravan, L. Blacker, D. P. Tew, D. L. Osborn, C. J. Percival, C. A. Taatjes, D. E. Shallcross and A. J. Orr-Ewing, ACS Earth Space Chem., 2018, 2, 833-842.
9. M. R. McGillen, B. F. E. Curchod, R. Chhantyal-Pun, J. M. Beames, N. Watson, M. A. H. Khan, L. McMahon, D. E. Shallcross and A. J. Orr-Ewing, ACS Earth Space Chem. , 2017, 1, 664-672.

10. R. Chhantyal-Pun, M. R. McGillen, J. M. Beames, M. A. Khan, C. J. Percival, D. E. Shallcross and A. J. Orr-Ewing, Angew. Chem. Int. Ed., 2017, 56, 9044-9047.
11. R. Chhantyal-Pun, A. Davey, D. E. Shallcross, C. J. Percival and A. J. Orr-Ewing, Phys. Chem. Chem. Phys., 2015, 17, 3617-3626.
12. T. Berndt, R. Kaethner, J. Voigtlander, F. Stratmann, M. Pfei, P. Reichle, M. Sipila, M. Kulmala and M. Olzmann, Phys. Chem. Chem. Phys. , 2015, 17, 19862-19873.
13. W. Chao, J.-T. Hsieh, C.-H. Chang and J. J.-M. Lin, Science, 2015, 347, 751.
14. T. R. Lewis, M. A. Blitz, D. E. Heard and P. W. Seakins, Phys. Chem. Chem. Phys., 2015, 17, 4859-4863.
15. L. Sheps, B. Rotavera, A. J. Eskola, D. L. Osborn, C. A. Taatjes, K. Au, D. E. Shallcross, M. A. H. Khan and C. J. Percival, Phys. Chem. Chem. Phys., 2017, 19, 21970-21979.
16. R. Chhantyal-Pun, O. Welz, J. D. Savee, A. J. Eskola, E. P. F. Lee, L. Blacker, H. R. Hill, M. Ashcroft, M. A. H. Khan, G. C. Lloyd-Jones, L. Evans, B. Rotavera, H. Huang, D. L. Osborn, D. K. W. Mok, J. M. Dyke, D. E. Shallcross, C. J. Percival, A. J. Orr-Ewing and C. A. Taatjes, J. Phys. Chem. A, 2017, 121, 4-15.
17. H.-L. Huang, W. Chao and J. J.-M. Lin, Proc. Natl. Acad. USA, 2015, 112, 10857-10862.
18. M. C. Smith, W. Chao, K. Takahashi, K. A. Boering and J. J.-M. Lin, J. Phys. Chem. A, 2016, 120, 4789-4798.
19. Y. Fang, F. Liu, V. P. Barber, S. J. Klippenstein, A. B. McCoy and M. I. Lester, J. Chem. Phys., 2016, 144, 061102.
20. V. P. Barber, S. Pandit, A. M. Green, N. Trongsiriwat, P. J. Walsh, S. J. Klippenstein and M. I. Lester, J. Am. Chem. Soc., 2018, 140, 10866-10880.
21. L. Vereecken, A. Novelli and D. Taraborrelli, Phys. Chem. Chem. Phys., 2017, 19, 31599-31612.
22. O. Welz, J. D. Savee, D. L. Osborn, S. S. Vasu, C. J. Percival, D. E. Shallcross and C. A. Taatjes, Science, 2012, 335, 204-207.
23. C. A. Taatjes, O. Welz, A. J. Eskola, J. D. Savee, A. M. Scheer, D. E. Shallcross, B. Rotavera, E. P. F. Lee, J. M. Dyke, D. K. W. Mok, D. L. Osborn and C. J. Percival, Science, 2013, 340, 177-180.
24. D. Stone, M. Blitz, L. Daubney, N. U. M. Howes and P. Seakins, Phys. Chem. Chem. Phys., 2014, 16, 1139-1149.
25. O. Welz, A. J. Eskola, L. Sheps, B. Rotavera, J. D. Savee, A. M. Scheer, D. L. Osborn, D. Lowe, A. M. Booth, P. Xiao, M. A. H. Khan, C. J. Percival, D. E. Shallcross and C. A. Taatjes, Angew. Chem. Int. Ed., 2014, 53, 4547-4550.
26. E. S. Foreman, K. M. Kapnas and C. Murray, Angew. Chem. Int. Ed., 2016, 55, 10419-10422.
27. S. V. Tadayon, E. S. Foreman and C. Murray, J. Phys. Chem. A, 2018, 122, 258-268.
28. X. Ge, A. S.Wexler and S. L.Clegg, Atmos. Environ., 2011, 45, 524-546.
29. Y. You, V. P. Kanawade, J. A. d. Gouw, A. B. Guenther, S. Madronich, M. R. Sierra-Hernández, M. Lawler, J. N. Smith, S. Takahama, G. Ruggeri, A. Koss, K. Olson, K. Baumann, R. J. Weber, A. Nenes, H. Guo, E. S. Edgerton, L. Porcelli, W. H. Brune, A. H. Goldstein and S.-H. Lee, Atmos. Chem. Phys., 2014, 14, 12181-12194.
30. X. Ge, A. S. Wexler and S. L. Clegg, Atmos. Environ., 2010, 45, 561-577.
31. O. Hertel, S. Reis, C. A. Skjøth, A. Bleeker, R. Harrison, J. N. Cape, D. Fowler, U. Skiba, D. Simpson, T. Jickells, A. Baker, M. Kulmala, S. Gyldenkærne, L. L. Sørensen and J. W. Erisman, Philos. T. Roy. Soc., 2013, 368, 177-207.
32. D. R. Hanson, P. H. McMurry, J. Jiang, D. Tanner and L. G. Huey, Environ. Sci. Technol., 2011 45, 8881-8888.
33. J. H. Zollner, W. A. Glasoe, B. Panta, K. K. Carlson, P. H. McMurry and D. R. Hanson, Atmos. Chem. Phys., 2012, 12 4399-4411.
34. F. J. Dentener and P. J. Crutzen, J. Atm. Chem., 1994, 19, 331-369.
35. S. Jørgensen and A. Gross, J. Phys. Chem. A, 2009, 113, 10284-10290.
36. J. P. Misiewicz, S. N. Elliott, K. B. M. III and H. F. S. III, Phys. Chem. Chem. Phys., 2018, 20, 7479-7491.
37. D. L. Osborn, P. Zou, H. Johnsen, C. C. Hayden, C. A. Taatjes, V. D. Knyazev, S. W. North, D. S. Peterka, M. Ahmed and S. R. Leone, Rev. Sci. Instrum., 2008, 79, 104103.
38. T. Banu, K. Sen and A. K. Das, J. Phys. Chem. A, 2018, 122, 8377-8389.
39. C. Hättig, D. P. Tew and A. Köh, J. Chem. Phys., 2010, 132, 231102.
40. D. P. Tew and W. Klopper, J. Chem. Phys., 2005, 123, 074101.
41. H.-J. Werner, P. J. Knowles, G. Knizia, F. R. Manby, M. Schütz, P. Celani, W. Györffy, D. Kats, T. Korona, R. Lindh, A. Mitrushenkov, G. Rauhut, K. R. Shamasundar, T. B. Adler, R. D. Amos, A. Bernhardsson, A. Berning, D. L. Cooper, M. J. O. Deegan, A. J. Dobbyn, F. Eckert, E. Goll, C. Hampel, A. Hesselmann, G. Hetzer, T. Hrenar, G. Jansen, C. Köppl, Y. Liu, A. W. Lloyd, R. A. Mata, A. J. May, S. J. McNicholas, W. Meyer, M. E. Mura, A. Nicklaß, D. P. O'Neill, P. Palmieri, K. Pflüger, R. Pitzer, M. Reiher, T. Shiozaki, H. Stoll, A. J. Stone, R. Tarroni, T. Thorsteinsson and M. Wang, MOLPRO, version 2015.1, a package of ab initio programs., http://www.molpro.net, 2015.
42. M. J. Frisch, G. W. Trucks, H. B. Schlegel, G. E. Scuseria, M. A. Robb, J. R. Cheeseman, G. Scalmani, V. Barone, B. Mennucci, G. A. Petersson, H. Nakatsuji, M. Caricato, X. Li, H. P. Hratchian, A. F. Izmaylov, J. Bloino, G. Zheng, J. L. Sonnenberg, M. Hada, M. Ehara, K. Toyota, R. Fukuda, J. Hasegawa, M. Ishida, T. Nakajima, Y. Honda, O. Kitao, H. Nakai, T. Vreven, J. A. Montgomery, J. E. P. Jr., F. Ogliaro, M. Bearpark, J. J. Heyd, E. Brothers, K. N. Kudin, V. N. Staroverov, R. Kobayashi, J. Normand, K. Raghavachari, A. Rendell, J. C. Burant, S. S. Iyengar, J. Tomasi, M. Cossi, N. Rega, J. M. Millam, M. Klene, J. E. Knox, J. B. Cross, V. Bakken, C. Adamo, J. Jaramillo, R. Gomperts, R. E. Stratmann, O. Yazyev, A. J. Austin, R. Cammi, C. Pomelli, J. W. Ochterski, R. L. Martin, K. Morokuma, V. G. Zakrzewski, G. A. Voth, P. Salvador, J. J. Dannenberg, S. Dapprich, A. D. Daniels, Ö. Farkas, J. B. Foresman, J. V. Ortiz, J. Cioslowski and D. J. Fox, Gaussian 09, Revision D.01, Gaussian, Inc., Wallingford CT, 2009.
43. D. R. Glowacki, C.-H. Liang, C. Morley, M. J. Pilling and S. H. Robertson, J. Phys. Chem. A, 2012, 116, 9545-9560.
44. S. J. Klippenstein and J. A. Miller, J. Phys. Chem. A, 2002, 106, 9267-9277.
45. M. J. Pilling and S. H. Robertson, Annu. Rev. Phys. Chem., 2003, 54, 245-275.
46. S. H. Robertson, M. J. Pilling, D. L. Baulch and N. J. B. Green, J. Phys. Chem. A, 1995, 99, 13452-13460.
47. Y. Liu, C. Yin, M. C. Smith, S. Liu, M. Chen, X. Zhou, C. Xiao, D. Dai, J. J.-M. Lin, K. Takahashi, W. Dong and X. Yang, Phys. Chem. Chem. Phys., 2018, 20, 29669-29676.
48. S. S. Brown, J. B. Burkholder, R. K. Talukdar and A. R. Ravishankara, J. Phys. Chem. A, 2001, 105, 1605-1614.
49. R. J. Shannon, M. A. Blitz, A. Goddard and D. E. Heard, Nature Chemistry, 2013, 5, 745-749.
50. R. Atkinson, D. L. Baulch, R. A. Cox, J. N. Crowley, R. F. Hampson, R. G. Hynes, M. E. Jenkin, M. J. Rossi and J. Troe, Atmos. Chem. Phys., 2004, 4, 1461-1738.

51. L. Onel, L. Thonger, M. A. Blitz, P. W. Seakins, A. J. C. Bunkan, M. Solimannejad and C. J. Nielsen, J. Phys. Chem. A, 2013, 117, 10736-10745.
52. D. Stone, L. K. Whalley and D. E. Heard, Chem. Soc. Rev., 2012, 41, 6348-6404.
53. A. Novelli, K. Hens, C. T. Ernest, M. Martinez, A. C. Nölscher, V. Sinha, P. Paasonen, T. Petäjä, M. Sipilä, T. Elste, C. Plass-Dülmer, G. J. Phillips, D. Kubistin, J. Williams, L. Vereecken, J. Lelieveld and H. Harder, Atmos. Chem. Phys., 2017, 17, 7807-7826.
54. B. Long, J. L. Bao and D. G. Truhlar, J. Am. Chem. Soc., 2016, 138, 14409-14422.
55. L.-C. Lin, H.-T. Chang, C.-H. Chang, W. Chao, M. C. Smith, C.-H. Chang, J. J.-M. Lin and K. Takahashi, Phys. Chem. Chem. Phys., 2016, 18, 4557-4568.
56. M. C. Smith, W. Chao, M. Kumar, J. S. Francisco, K. Takahashi and J. J.-M. Lin, J. Phys. Chem. A, 2017, 121, 938-945.
57. M. Kumar and J. S. Francisco, Angew. Chem. Int. Ed., 2016, 55, 13432-13435.
58. Y.-H. Lin, C. Yin, W.-H. Lin, Y.-L. Li, K. Takahashi and J. J.-M. Lin, J. Phys. Chem. Lett., 2018, 9, 7040-7044.
59. S. W. Benson, J. Chem. Edu., 1965, 42, 502-518.

